

# Reconstructions in limited-view thermoacoustic tomography

Yuan Xu and Lihong V. Wang<sup>a)</sup>

*Optical Imaging Laboratory, Department of Biomedical Engineering, Texas A&M University, 3120 TAMU, College Station, Texas 77843-3120*

Gaik Ambartsoumian and Peter Kuchment

*Department of Mathematics, Texas A&M University, College Station, Texas 77843-3368*

(Received 4 September 2003; revised 5 December 2003; accepted for publication 9 December 2003; published 11 March 2004)

The limited-view problem is studied for thermoacoustic tomography, which is also referred to as photoacoustic or optoacoustic tomography depending on the type of radiation for the induction of acoustic waves. We define a “detection region,” within which all points have sufficient detection views. It is explained analytically and shown numerically that the boundaries of any objects inside this region can be recovered stably. Otherwise some sharp details become blurred. One can identify in advance the parts of the boundaries that will be affected if the detection view is insufficient. If the detector scans along a circle in a two-dimensional case, acquiring a sufficient view might require covering more than a  $\pi$ -, or less than a  $\pi$ -arc of the trajectory depending on the position of the object. Similar results hold in a three-dimensional case. In order to support our theoretical conclusions, three types of reconstruction methods are utilized: a filtered backprojection (FBP) approximate inversion, which is shown to work well for limited-view data, a local-tomography-type reconstruction that emphasizes sharp details (e.g., the boundaries of inclusions), and an iterative algebraic truncated conjugate gradient algorithm used in conjunction with FBP. Computations are conducted for both numerically simulated and experimental data. The reconstructions confirm our theoretical predictions. © 2004 American Association of Physicists in Medicine.  
[DOI: 10.1118/1.1644531]

Key words: thermoacoustic tomography, photoacoustic tomography, optoacoustic tomography, local tomography, limited view, incomplete data

## I. INTRODUCTION

A correlation between the electromagnetic absorption of a biological tissue and its physiological and pathological features is reported.<sup>1-4</sup> To employ this contrast mechanism, thermoacoustic tomography (TAT), in which the thermoacoustic signals from a tissue sample are collected to map the distribution of the radiation absorption within the sample, has been developed to image biological tissue.<sup>5-9</sup> TAT, which is also referred to as photoacoustic or optoacoustic tomography (depending on the type of radiation used), combines good imaging resolution with good imaging contrast.

As it will be shown below, TAT signals can be represented in terms of a known circular radon transform. There exist explicit reconstruction formulas for this transform when data are collected along a line or a full circle in a two-dimensional (2-D) case and along a plane, sphere, or a cylinder in a three-dimensional (3-D) case.<sup>10-15</sup> In all these cases it is assumed that the imaged objects are located either on one side of the scanning line (plane), or inside the scanning circle (sphere, cylinder), without which assumption reconstruction is not always possible. The available inversion formulas employ either special-function expansions, or backprojection in the case of the linear or planar data-acquisition geometry.

Exact reconstruction algorithms for TAT based on series-expansion techniques are implemented in planar, spherical, and cylindrical configurations.<sup>5-7,16</sup> Following the line of

Norton,<sup>17</sup> an approximate modified backprojection algorithm has been developed from an exact 3-D model.<sup>6</sup> Other backprojection algorithms are also proposed.<sup>8,18</sup> In these algorithms for TAT, it is assumed that the thermoacoustic signals are detected in a full (panoramic) view. In other words, the detector moves along a whole circle in the 2-D case or sphere in the 3-D case. This means in particular that each point of the scanned object is visible from the detector's trajectory for  $2\pi$  radians in the 2-D case or  $4\pi$  steradians in the 3-D case. However, in many applications of TAT, the signals cannot be collected from all directions. For example, the solid angle of detection is at most  $2\pi$  steradians for a breast. So, one faces here an incomplete data problem. Although one can show that theoretically an arbitrarily small scanning arc (i.e., the arc of a circle over which the detectors move) suffices for the uniqueness of recovery,<sup>22</sup> in practical implementations the limited-view problems usually lead to losing some parts of the high-frequency information and hence blurring of some sharp details.

In this paper, we present our results on the limited-view TAT. Although limited-view problems have been studied extensively in x-ray tomography,<sup>19</sup> diffraction tomography,<sup>20</sup> and reflectivity tomography,<sup>21</sup> to the best of our knowledge, no results on the limited-view TAT have been published. In the methods section, a formula for the forward problem is presented. In particular, it is shown that the TAT signals can

be represented in terms of a known circular radon transform. This enables us to employ the known results that justify the theoretical possibility of reconstruction.<sup>22</sup> Then results by Quinto and Louis developed for sonar are applied to determine the “stably visible” parts of the objects in TAT.<sup>23</sup> In particular, a piece of the boundary of an object (i.e., interfaces between objects) can be stably reconstructed as soon as at any point on the boundary at least one of its two normal directions passes through a detector position. On an intuitive level, this is because an arbitrary interface can be considered as a combination of small flat interface segments, and each segment transmits acoustic waves identically in the two opposite directions perpendicular to the interface segment. This means that we need to collect signals at only one of the two directions to obtain information about the boundary segment. More complicated sharp details (“singularities”) could be considered as well, which would entail using the notion of a wavefront of a function and other tools of microlocal analysis. However, among all possible singularities, tissue interfaces are of the most interest for TAT.

Exact reconstruction formulas for the limited-view TAT are not yet known. We derive an approximate filtered back-projection (FBP) algorithm that works well quantitatively. A version of this method that emphasizes singularities [a “local tomography” (LT) reconstruction] is also tested. The FBP results are then iteratively improved using a truncated conjugated gradient (TCG) method. Besides using numerical phantoms for calculations, we also conducted experimental measurements on physical phantoms and applied our reconstruction methods to the obtained data. The results of all these reconstructions confirm our theoretical predictions. These are addressed in the Sec. III.

## II. METHODS

### A. Formulas for the forward problem

We begin by presenting the forward problem for an acoustically homogeneous model. In the case of thermal confinement, the spectrum of the acoustic wave pressure  $\bar{p}(\mathbf{r}, k)$  at a detector position  $\mathbf{r}$  is related to the spatial distribution of electromagnetic absorption  $\varphi(\mathbf{r}')$ ,<sup>5</sup>

$$\bar{p}(\mathbf{r}, k) = \frac{iv_s \beta I_0 k \bar{\eta}(k)}{4\pi C} \times \oint \varphi(\mathbf{r}') \frac{\exp(-ik|\mathbf{r}-\mathbf{r}'|/v_s)}{|\mathbf{r}-\mathbf{r}'|} d\mathbf{r}'. \quad (1)$$

Here  $k$  is the angular frequency with respect to  $t$ ;  $v_s$  is the acoustic speed;  $C$  is the specific heat;  $\beta$  is the coefficient of volumetric thermal expansion;  $I_0$  is a scaling factor proportional to the incident radiation intensity;  $\varphi(\mathbf{r}')$  describes the to-be-reconstructed electromagnetic absorption property of the medium at  $\mathbf{r}'$ ; and  $\bar{p}(\mathbf{r}, k)$  and  $\bar{\eta}(k)$  are the temporal Fourier transforms of the pressure  $p(\mathbf{r}, t)$  and the shape of the irradiating pulse  $\eta(t)$ , respectively.

Defining  $\bar{p}_1(\mathbf{r}, k) = \bar{p}(\mathbf{r}, k)/\bar{\eta}(k)$  and applying inverse Fourier transform, one obtains

$$p_1(\mathbf{r}, t) = \frac{v_s \beta I_0}{4\pi C} \frac{\partial}{\partial t} \oint_{t=|\mathbf{r}-\mathbf{r}'|/v_s} \frac{\varphi(\mathbf{r}')}{|\mathbf{r}-\mathbf{r}'|} d\mathbf{r}', \quad (2)$$

where  $p_1(\mathbf{r}, t)$  is the deconvolution of  $p(\mathbf{r}, t)$  with respect to the profile of the electromagnetic pulse and can be interpreted as the detected pressure when the electromagnetic pulse is a delta (impulse) function. The physical meaning of this equation is that, in an acoustically homogeneous medium, the pressure  $p_1$  at a spatial point  $\mathbf{r}$  and time  $t$  is proportional to the time derivative of the integral of the absorbed electromagnetic energy over a spherical surface (a circle in the 2-D case) centered at  $\mathbf{r}$  and with a radius of  $tv_s$ :

$$|\mathbf{r}-\mathbf{r}'| = tv_s. \quad (3)$$

2-D TAT is studied in our numerical simulations and experiments. It should be pointed out that 2-D TAT is valid for experimental configurations where thermoacoustic sources are approximately located within a thin slab or the ultrasonic transducers are cylindrically focused to select thermoacoustic sources from a thin slab.

### B. Analysis of singularities in circular radon transform and limited-view TAT

#### 1. Circular radon transform

It can be seen from Eq. (2) that  $p_1(\mathbf{r}, t)$  can be obtained from  $\varphi(\mathbf{r}')$  after applying three linear operations: circular (spherical in 3-D) radon transform  $\mathbf{R}$ , multiplication by  $1/t$ , and differentiation  $\mathbf{D}_t$  with respect to  $t$ . The circular radon transform defined as

$$\mathbf{R}\varphi(\mathbf{r}, t) = \oint_{t=|\mathbf{r}-\mathbf{r}'|/v_s} \varphi(\mathbf{r}') d\mathbf{r}' \quad (4)$$

is similar to the conventional linear radon transform, except that the integration here is over a circle or a sphere rather than a line or a plane. In this paper, the set  $\Sigma$  of centers  $\mathbf{r}$  of the circles (spheres) of integration coincides with the set of positions of the detector, and the set of radii (that are proportional to time  $t$ ) is unrestricted. We call these circles (spheres) “projection curves” (“projection surfaces”) and the set  $\Sigma$  the “scanning curve” (or “detector curve”). We assume that the source function  $\varphi(\mathbf{r})$  is zero outside  $\Sigma$  and in a neighborhood of  $\Sigma$ . In other words, the scanned object is strictly inside the scanning detector trajectory  $\Sigma$ . In this case it is known that data collected from an arbitrarily small arc of the detector trajectory are theoretically sufficient for a complete reconstruction.<sup>22</sup> This result, however, neither provides reconstruction algorithms, nor guarantees that the reconstruction can be achieved in any practically stable manner. Indeed, it is well known that solving incomplete data problems usually leads to operations like Fourier filtrations with fast growing filters,<sup>15</sup> which implies high sensitivity to errors in data. This in turn requires cutting high frequencies and hence blurring the images. Sacrifices in high frequencies naturally lead to destroying sharp details (interfaces between different tissues) in the reconstruction. The question of what parts of

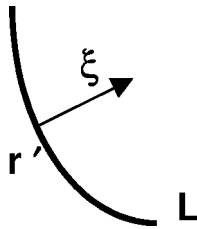


FIG. 1. Wavefront  $WS(\varphi)$  of an image  $\varphi$  consisting of pairs  $(\mathbf{r}', \xi)$ , where point  $\mathbf{r}'$  belongs to  $\mathbf{L}$  (a jump interface in the image) and  $\xi$  is a nonzero vector normal to  $\mathbf{L}$  at  $\mathbf{r}'$ .

the singularities (i.e., sharp details) of the image can be stably reconstructed depending on the scanning geometry is addressed for the planar radon transform,<sup>24</sup> and for the circular one in connection with sonar.<sup>23</sup> Local tomography reconstructions also address similar issues.<sup>25–28</sup>

## 2. TAT

We would like to note that in Eq. (2) the presence of a temporal derivative in the TAT data (which is equivalent to a radial derivative after the circular radon transform) can only emphasize singularities and hence should not lead to additional blurring in comparison with the circular radon transform itself (this can be shown rigorously). In fact, as it will be seen later in this paper, this derivative is a natural part of the reconstruction procedure for the circular radon transform.

We will now apply to TAT the known results of integral geometry concerning singularity reconstruction.<sup>23,24</sup> The exact description would require the notions of microlocal analysis, in particular the one of a wavefront set of a function.<sup>23,24</sup> However, in tomographic problems, in particular in TAT, one is mostly interested in only one type of singularity: the jump of the imaged value  $\varphi$  across an interface (a curve in 2-D or a surface in 3-D). Assuming that  $\varphi$  is smooth except for a jump across a curve  $\mathbf{L}$  in the plane (the 3-D situation is analogous with  $\mathbf{L}$  being a surface), then the wavefront  $WS(\varphi)$  of  $\varphi$  consists of pairs  $(\mathbf{r}', \xi)$  where point  $\mathbf{r}'$  belongs to  $\mathbf{L}$  and  $\xi$  is a nonzero vector normal to  $\mathbf{L}$  at  $\mathbf{r}'$  as shown in Fig. 1.

Now Louis' results can be summarized as follows:<sup>23</sup> one can identify that a pair  $(\mathbf{r}', \xi)$  belongs to the wavefront set of the image by looking at the singularities of the radon data if and only if among the circles (spheres) of integration (“projection curves”) there exists at least one passing through the point  $\mathbf{r}'$  and normal to  $\xi$  at this point. To put it differently, in TAT one can see without blurring only those parts of the interfaces that one can touch tangentially by circles (spheres) centered at detector positions. This means that one needs to have a detector located on the normal to  $\mathbf{L}$  at  $\mathbf{r}'$  in either direction.

What happens to other, “invisible” parts of the interfaces? We provide here a nontechnical explanation. One would need to recover these singularities from smooth parts of the measured data. This in turn means the involvement of operations like filtrations in the frequency domains with filters growing faster than any power. In order to avoid instabilities

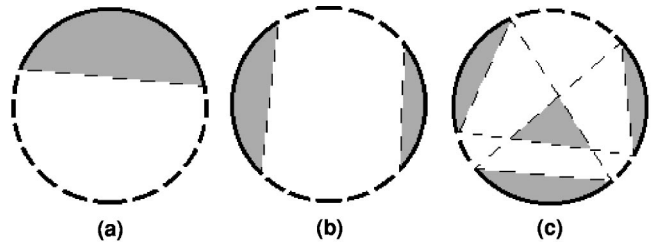


FIG. 2. (a) An illustration of the “detection regions” (shaded areas) of circular radon transform, when the detector moves along a single arc (solid) of a circle. (b) Two arcs. (c) Three arcs.

then, this clearly requires cutting those frequencies off, which causes blurring. The conclusion is that the “visible” parts of the interfaces should be possible to recover, while the others should blur independently of the reconstruction method used. A discussion of the related issues of stability of reconstruction would be too lengthy; one can find the relevant considerations in the literature.<sup>29</sup> In a nutshell, more stable tomographic problems allow one to estimate the error in the reconstruction (in a Sobolev norm) by the error in the data in a somewhat smoother norm. This, however, is impossible when the information about the wavefront is lost.

Let us make this geometry more explicit for our circular (spherical) trajectory of detectors. We pose the following question: Assume that only a part of the detector circle (sphere) is used for collecting data; at what locations then, all interfaces in the image will be completely recoverable? We will call the set of all such “good” locations the “detection region.” For images outside this region, one needs to apply the tangent-circle test as described in the preceding two paragraphs to predict what parts of the boundaries will not be stably recoverable.

Assuming first that the detector moves along a single arc of the circle [Fig. 2(a)], then simple geometric consideration shows that the “detection region” is just the convex hull of this arc (i.e., the circular cap based on the arc). Here the “detection region” is shaded, and the arc of the circle where we do not position a detector is shown as a dotted line. Analogously, one can find the “detection region” (shaded) for two arcs [Fig. 2(b)]. The situation changes, however, for more complicated scanning trajectories. For instance, in the case of three arcs, one can have more than just circular caps in the “detection region” [Fig. 2(c)]. Here an additional triangular part of the “detection region” appears in the center. The situation can become even more complicated for spherical 3-D geometry. The general rule for finding the “detection region” is as follows: draw all lines such that both of their intersection points with the scanning circle (sphere) do not coincide with detector locations. These lines cover the “invisible” domain, so its complement forms the “detection region.” Note that in the “invisible” domain some boundaries can still be recovered stably, while others blur away. Namely, the parts of the boundaries the normal lines to which pass through a detector position, and only those can be stably recoverable. The above conclusions are illustrated in Fig. 3, where the “invisible” parts of the object boundaries, i.e., the

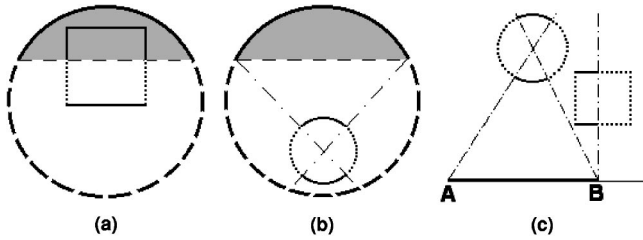


FIG. 3. (a) “Visible” (solid line) and “invisible” (dashed) boundaries of a square object, and the “detection regions” (shaded areas) when the detector moves along an arc (solid). (b) The same as (a) for a disk phantom. (c) The same as (a) except that the detector moves along the line segment  $AB$  and the objects are a square and a disk. The “visible” boundaries are expected to be recoverable stably, while the “invisible” boundaries should be blurred away.

ones to be blurred during the reconstructions, are shown with dotted lines. For instance, in Fig. 3(a) one has a cap “detection region” and a rectangular object that does not fit fully into it. Then one expects the dotted parts of the rectangle’s boundary to be affected by blurring artifacts during the reconstruction. Figure 3(b) shows the expected reconstruction of a circular object located outside the “detection region.” Let us remark that similar considerations apply to an arbitrary scanning geometry. For instance, Fig. 3(c) shows the parts (solid) of the boundaries of a circular and a square object that can be stably reconstructed from the detection on a segment  $AB$ .

**C. Reconstruction methods**

As it has already been mentioned before, exact inversion procedures are known for circular and spherical radon transforms in some special detection configurations.<sup>10–15</sup> However, for the circular trajectories of detectors only special-function-expansion methods are known, while formulas of the FBP type are available for the linear (planar) trajectories. Our approach is to use an approximate FBP formula, which happens to work well under most circumstances and can be improved in conjunction with post-processing by an iterative method. Namely, for objects not too close to the detectors, one can think of projection lines as close to straight lines, and hence the circular radon transform as being close to the standard radon transform. In this approach, the center  $\mathbf{r}$  of the projection circle and its radius  $\rho$  (which is proportional to time) are analogs of the normal coordinates  $(\hat{\theta}, \varsigma)$  of a line  $\mathbf{r} \cdot \hat{\theta} = \varsigma$  in the standard radon transform where  $\hat{\theta}$  is a unit vector normal to the line. FBP inversion of the standard radon transform on the plane consists (up to a constant factor) in applying the first derivative with respect to  $\varsigma$ , then Hilbert transform with respect to  $\varsigma$ , and finally the backprojection operator, which averages over lines passing through a given point.<sup>15</sup> We implement a similar procedure in the circular radon transform. This amounts to a differentiation with respect to the radius, a Hilbert transform with respect to the radius, and then a circular backprojection, i.e., averaging over the circles passing through a given point. One should also make sure that during the backprojection the tangent

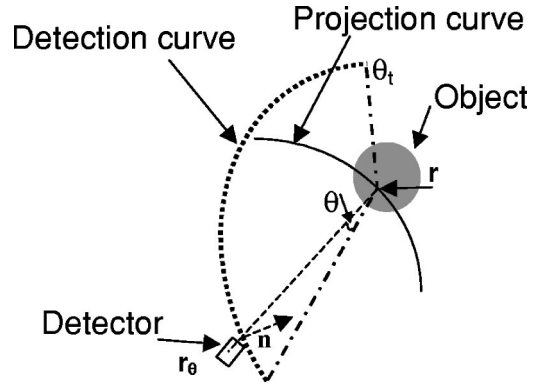


FIG. 4. A diagram to show the uniform rotation of  $\theta$  in FBP in a circular radon transform or TAT. The dashed arrow represents the normal to the detection curve (dotted arc) at  $\mathbf{r}_\theta$  and the dashed line is the normal to a projection arc centered at  $\mathbf{r}_\theta$  and passing through a reconstructed point  $\mathbf{r}$ .  $\theta_t$  is the detection view at  $\mathbf{r}$ , i.e., the angle subtended by the detection curve as viewed from  $\mathbf{r}$ .

lines (or the normal vectors) to the projection curves at the given point, for example,  $\theta$  in Fig. 4, rather than the centers of the projection curves (which coincide with detector positions), rotate at a constant speed. Differentiation with respect to the radius is already contained in the TAT data, as shown in Eq. (2), so this step can be simplified in 2-D reconstructions (it is still required in a 3-D TAT). Based on this, we arrive in the Appendix at an approximate FBP reconstruction formula for the 2-D TAT,

$$\varphi(\mathbf{r}) \approx \frac{C}{\beta I_0 v_s^2} \oint ds \frac{\mathbf{n} \cdot (\mathbf{r} - \mathbf{r}_\theta)}{|\mathbf{r} - \mathbf{r}_\theta|^2} \mathbf{H}(p_1(\mathbf{r}_\theta, |\mathbf{r}_\theta - \mathbf{r}|/v_s) \times |\mathbf{r} - \mathbf{r}_\theta| + p_2(\mathbf{r}_\theta, |\mathbf{r}_\theta - \mathbf{r}|/v_s)), \tag{5}$$

where  $\mathbf{H}$  is a Hilbert transform;  $p_2(\mathbf{r}, t) = v_s \int_0^t p_1(\mathbf{r}, t) dt$ ;  $\mathbf{n}$  is the inward normal to the detection curve at  $\mathbf{r}_\theta$ ;  $ds$  is the arc length differential; and the integration is along a complete detection curve (i.e., the one that runs around the objects). In the case of incomplete data, one just replaces the missing data with zeros (possibly gradually phasing off the existing data closely to the missing data region to reduce the artifacts caused by the missing data) and then applies the formula. Although this is not an exact inversion, one can show using microlocal analysis that it preserves all “visible” singularities (a conclusion supported by the numerical and experimental evidences presented below). If one is interested in singularities only (e.g., interfaces between different types of tissue), then one can drop the integral term  $p_2(\mathbf{r}_\theta, |\mathbf{r}_\theta - \mathbf{r}|/v_s)$  in the last formula, since it corresponds to a pseudo-differential operator of a smaller order.

Let us also provide a local tomography formula for the 2-D TAT. In order to do this we replace the Hilbert transform by an additional time derivative. This then leads to the local tomography reconstruction:

$$\Lambda \varphi(\mathbf{r}) = \frac{C}{\beta I_0 v_s^2} \oint ds \frac{\mathbf{n} \cdot (\mathbf{r} - \mathbf{r}_\theta)}{|\mathbf{r} - \mathbf{r}_\theta|^2} \left( \frac{\partial p_1}{\partial t}(\mathbf{r}_\theta, |\mathbf{r}_\theta - \mathbf{r}|/v_s) \times |\mathbf{r} - \mathbf{r}_\theta| + 2v_s p_1(\mathbf{r}_\theta, |\mathbf{r}_\theta - \mathbf{r}|/v_s) \right). \tag{6}$$

As before, if one wants to recover singularities only, the term of a lower pseudo-differential order  $2\nu_s p_1$  in this formula can be dropped.

One can apply a similar consideration to the 3-D TAT, which leads to the approximate FBP formula:

$$\begin{aligned} \varphi(\mathbf{r}) \approx & -\frac{C}{2\pi\beta I_0 v_s^3} \oint dS \frac{\mathbf{n} \cdot (\mathbf{r} - \mathbf{r}_\theta)}{|\mathbf{r} - \mathbf{r}_\theta|^2} \\ & \times \left( \frac{\partial p_1(\mathbf{r}_\theta, |\mathbf{r}_\theta - \mathbf{r}|/v_s)}{\partial t} + \frac{2p_1(\mathbf{r}_\theta, |\mathbf{r}_\theta - \mathbf{r}|/v_s)v_s}{|\mathbf{r}_\theta - \mathbf{r}|} \right). \end{aligned} \quad (7)$$

In the case of limited-angle detection, there is also the following possibly useful correction if one is interested in quantitative imaging. Here, we define a detection view  $\theta_t$  (solid angle  $\Omega_t$  for the 3-D case) at  $\mathbf{r}$ , which is the (solid) angle subtended by the detection curve (surface) when viewed from the reconstruction point  $\mathbf{r}$  as shown in Fig. 4. Because of the incompleteness of data, the integral in the above equations runs over a portion of the detection curve (surface) only. One might want to compensate for that by multiplying the value of the reconstructed function at this point by a factor  $2\pi/\theta_t$  ( $4\pi/\Omega_t$  for the 3-D case). The factor appears when the backprojection operator is considered approximately as an averaging over the available projection curves passing through the reconstruction point  $\mathbf{r}$ . It should be noted that both  $\theta_t$  and  $\Omega_t$  depend on  $\mathbf{r}$ . The effectiveness of this compensation is shown below by our numerical simulation results of TAT.

There are three useful features of Eq. (5) and Eq. (7). First of all, they yield, as we intend to show in numerical simulations, acceptable quantitative results from limited-view data. Second, their computation complexity is much less than that for the iterative methods such as TCG, while they produce images of comparable quality. Finally, if an iterative method is necessary, our backprojection formula can serve as a good initial guess. This is also observed in our numerical simulations.

Although the above backprojection formula is shown to work well in numerical simulations, it is not exact. Nevertheless, one can show that it amounts to applying a pseudo-differential operator to the image  $\varphi$  (this is true if the data is gradually phased out near the areas of the missing data). Pseudo-differential operators are known not to shift locations of any singularities, including boundaries.<sup>19,28,30</sup> This means that although the backprojection formula might give imprecise values of  $\varphi$ , it will present the locations of the boundaries of all inclusions correctly.

Another reconstruction method is to apply an additional differentiation with respect to time (the radius) without applying a Hilbert transform, as shown in Eq. (6). This leads to a local tomography type formula.<sup>25,28</sup> The result of the procedure also produces an expression of the form  $\Lambda\varphi$ , where  $\Lambda$  is a pseudo-differential operator defined in Eq. (6). In this case, however, the operator has a positive order, which means that all the “visible” interfaces and other sharp details not only have correct locations, but also are emphasized.

This effect is well known in image processing, where for instance the Laplace operator is sometimes used to emphasize the edges. One can also notice that our experimental data, due to the shape of the transducer’s impulse response function and electromagnetic pulse shape, already carry a filtration that makes the reconstruction similar to the local one. Then, unless an appropriate deconvolution is applied to the data during pre-processing, the interfaces are accentuated in the reconstruction. The reader will notice this in our actual reconstructions from experimental data.

#### D. Numerical implementation

In the case of incomplete data discussed above, we complete it by concatenating with zeros (sometimes gradually smoothing the data to zero at the boundary in order to reduce the artifacts in the reconstruction). The FBP algorithm described above is first applied to the limited view data. Since the inversion formula we use is not exact even for complete data, we improve it by employing an iterative algebraic method for solving the discretized version of Eq. (2), starting with the FBP reconstruction as the initial guess. We adopt as such the TCG method for finding the least-squares solution of the discretized version of the problem. No preconditioner is used. We also employ local tomography procedure described above. We expect in all these methods to see the reconstructions that agree with the theoretical predictions stated in the previous section, i.e., sharp “visible” details with the “invisible” parts blurred.

### III. RESULTS AND DISCUSSION

Our results consist of three parts: (1) inversion of simulated circular radon transform data to show the theoretical predictions about the “visible” and “invisible” boundaries, (2) reconstructions from simulated TAT data to test our reconstruction algorithms quantitatively, and (3) images based on experimental data collected from a physical phantom.

#### A. Numerical results for the limited-view circular radon transform

Figure 5 shows the inversion of the circular radon transform for different detection configurations and phantoms (shown in the first column from the left) to demonstrate our discussions on the “visible” and “invisible” boundaries. In the second column from the left, the detection curve is shown as the solid part of the outer circle, the “detection region” is shaded, and the “visible” (solid) and “invisible” (dashed) boundaries of the objects predicted by theory are shown. The inclusion represents the object to be imaged. The third and fourth columns from the left show the FBP reconstructions and the local tomography reconstructions, respectively. Notice the good agreement between the three columns on the right concerning reconstructions of the “visible” and “invisible” parts of the boundaries.

Figure 5(1a–1d) shows the results for a phantom containing a square inclusion. The data are collected from detectors located on the upper half-circle. Exactly the parts of the

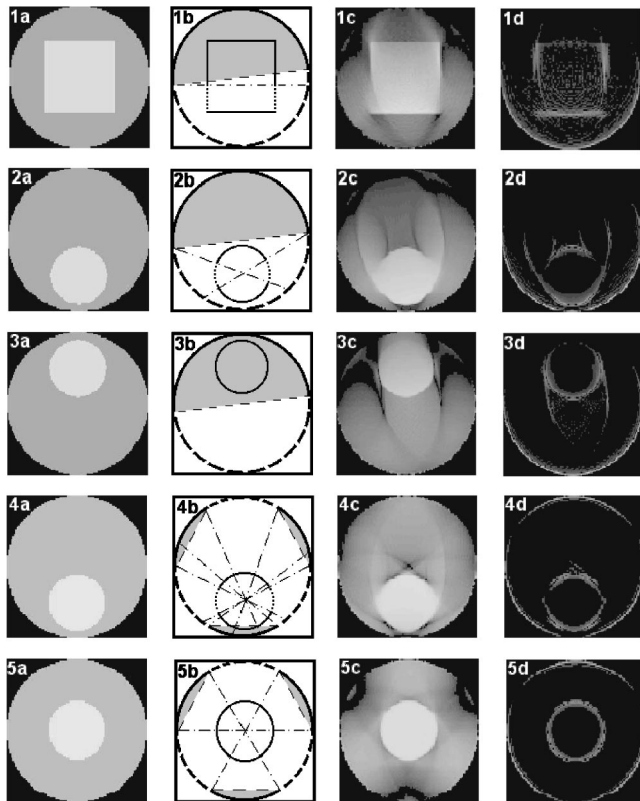


FIG. 5. (1a) A square phantom inside a circular detection curve in a circular radon transform. (1b) The diagram showing the detection curve (solid part of the outer circle), the “visible” (solid) and “invisible” (dashed) boundaries of the object predicted by theory, and the “detection region” (shaded). (1c) FBP reconstruction. (1d) Local tomography reconstruction, where the boundary is emphasized. (2a–2d) A disk phantom outside the “detection region.” (3a–3d) A disk phantom inside the “detection region.” (4a–4d) An off-center disk phantom and a detection curve consisting of three arcs. (5a–5d) A centered disk phantom and a detection curve consisting of three arcs.

boundary of the square predicted in this paper [see the dotted lines in Fig. 5(1b)] become blurred in Fig. 5(1c) and Fig. 5(1d).

Figure 5(2a–2d) and Fig. 5(3a–3d) show the reconstructions of circular inclusions from the data collected by the detector located along the upper half-circle. In Fig. 5(2a–2d), the phantom is completely outside the “detection region,” which leads to blurring of its right and left boundaries in accordance with the theory. In Fig. 5(3a–3d), however, the boundaries of the disk are recovered sharply, since the inclusion is in the “detection region.” Notice here some deterioration of the image near the detector circle. This can be attributed to the fact that near the detector circle, linear, and circular radon transform become noticeably different, and so the quality of our approximate formulas diminishes. This problem can be dealt with in two ways: one can make sure that the detectors do not approach the imaged objects too closely (this will be enforced in our further numerical simulations and experiments), or to improve the reconstruction quality by post-processing with an iterative algebraic reconstruction method.

Other limited-view reconstructions from the circular radon data are shown in Fig. 5(4a–4d) and Fig. 5(5a–5d),

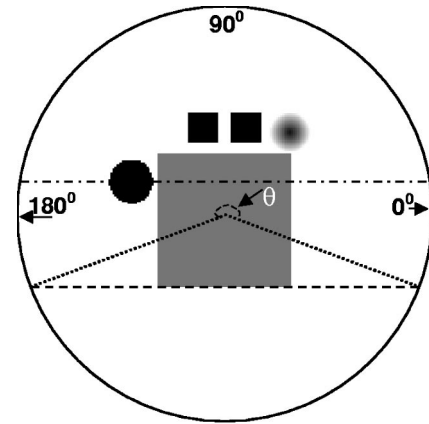


FIG. 6. A diagram of inclusions in TAT (used in Fig. 7). The value of the image  $\varphi(\mathbf{r})$  is set to be 0.5 in the largest square and unity within other sharp inclusions and zero elsewhere. Inside the “soft” circular inclusion, this value drops linearly with the radius from unity at the center to zero at the interface.

where there are three arcs of detection, 60 degrees each, with 60 degrees intervals between them. An off-center and a centered circular inclusion are reconstructed in Fig. 5(4a–4d) and Fig. 5(5a–5d), respectively. The results agree well with the theory: some parts of the boundary of the off-center disk are blurred; namely, those where the normals do not pass through any detector positions. However, the in-center disk is reconstructed sharply, in spite of the fact that it does not fit into the “detection region.” The reason is that in this case every normal to the boundary of the inclusion passes through a detector.

## B. Reconstruction from simulated limited-view TAT data

A numerical phantom that contains four sharp and one soft inclusions is shown in Fig. 6. Among the sharp ones we have one large and two small squares and one disk. The object value, which represents the electromagnetic energy deposition, is set to be 0.5 within the largest square and unity within other sharp inclusions and zero elsewhere. Inside the “soft” circular inclusion, this value drops linearly with the radius from unity at the center to zero at the interface in order to simulate a gradual interface. The imaged field of 154 mm by 154 mm is mapped with a  $128 \times 128$  mesh. The detection circle has a radius of 133 mm and is centered at the center of the picture. We scan 200 steps in all the simulations. The gray scale and the scale bar of the images are shown below the images in Fig. 7. The top row of reconstructions employs the local tomography formula that emphasizes the boundaries. The next one uses the FBP formula, and the lowest one shows the improvements achieved by running the algebraic reconstruction method (TCG) starting with the FBP as an initial guess.

The left column uses only the data collected from the  $\pi/2$  detection arc in the first quadrant. None of the phantom inclusions fits into the “detection region.” One can see that all parts of the inclusion boundaries the normals to which do not intersect the detector arc are blurred (even in the local to-

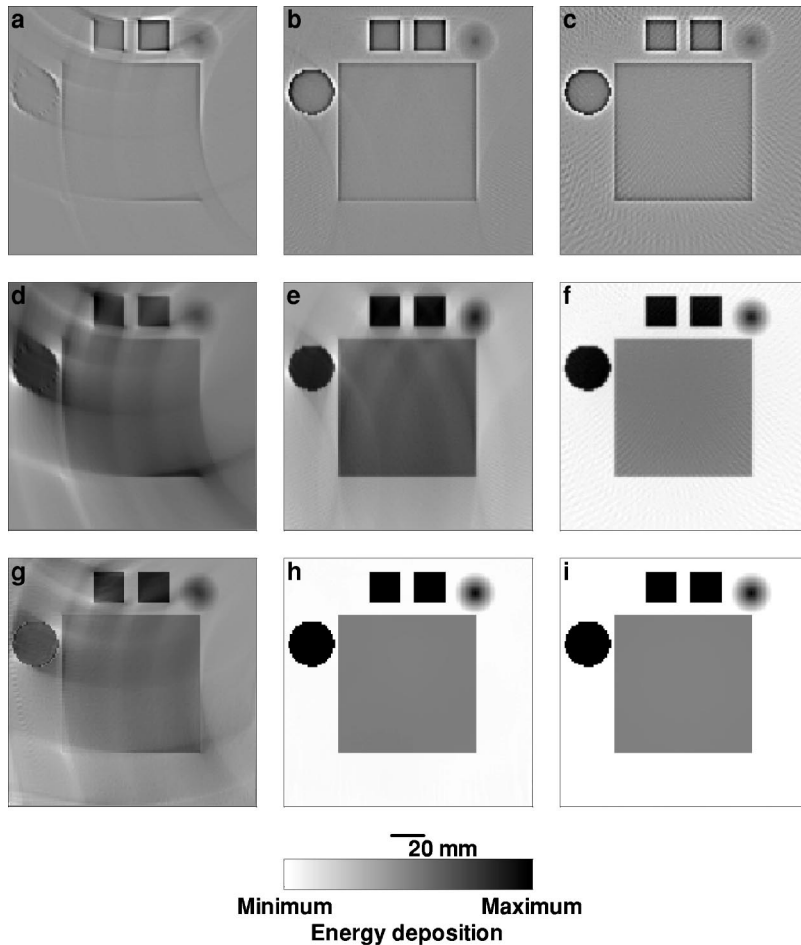


FIG. 7. Images reconstructed from simulated TAT data corresponding to the phantom in Fig. 6. The three columns correspond from the left to the right to detection angles of 90 degrees (from  $0^\circ$  to  $90^\circ$ ), 217 degrees (from  $-19^\circ$  to  $198^\circ$  as shown by the angle  $\theta$  in Fig. 6), and 360 degrees, respectively. The three rows correspond from top to bottom to the local tomographic reconstruction, FBP, and FBP with the consecutive TCG, respectively. The values of (minimum, maximum) of the gray scale for (a)–(i) are  $(-0.8081, 1.0000)$ ,  $(-0.8302, 1.0000)$ ,  $(-0.7515, 1.0000)$ ,  $(-2.0745, 1.7899)$ ,  $(-0.6385, 1.0723)$ ,  $(-0.1030, 1.0349)$ ,  $(-0.9284, 1.2859)$ ,  $(-0.0326, 1.0030)$ , and  $(-0.0149, 1.0021)$ , respectively. The maxima of the local reconstructions are normalized to unity.

mography reconstruction). Other parts of the boundaries are sharp. This is in perfect agreement with our theoretical prediction. The soft inclusion is not significantly affected by the artifacts.

The middle column employs the data collected from the detector arc of approximately 217 degrees (the angle  $\theta$  in Fig. 6), whose chord coincides with the bottom side of the large square inclusion. In this case all inclusions are in the “detection region,” and hence all the boundaries are reconstructed sharply. The third column represents the full data reconstruction. Notice that the quality of the final reconstructions in the last two columns is the same.

Figures 8(a) and 8(b) show the reconstructed image  $\varphi(\mathbf{r})$  along the dashed–dotted line in Fig. 6 using the FBP [Figs. 7(d)–7(f)] and TCG reconstructions [Figs. 7(g)–7(i)], respectively. The exact value is also shown for comparison. It can be found in Fig. 8(a) that the results of FBP are in good agreement with the real value for the case of 217-degree and 360-degree detection, where all objects are in the “detection region.” Iteration improves the results further as shown in Fig. 8(b). Even for the case of a 90-degree detection curve, the profile of the objects is reconstructed. Comparing (a) and (b), one can find that the significant overshoot and undershoot in FBP can be considerably reduced by TCG iterations (we remind the reader that FBP is only an approximation rather than the implementation of an exact formula).

### C. Dependence of reconstruction on scanned angular range

Figure 9 shows the relative error of each reconstruction as a function of the scanned angular range with respect to the center of the scan. We study the mean reconstruction values in the hard sphere, the central square, and the background. The errors of reconstruction are normalized to the corresponding real values in the cases of the hard sphere and the central square and to the real value of the hard sphere in the

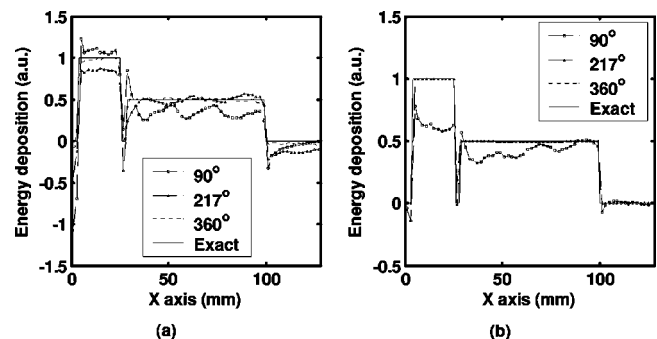


FIG. 8. (a) The graphs of FBP reconstructions shown in Figs. 7(d)–7(f) and the corresponding exact value along the dashed–dotted line in Fig. 6. (b) The graphs corresponding to TCG reconstructions, Figs. 7(d)–7(f), along the same line as in (a).

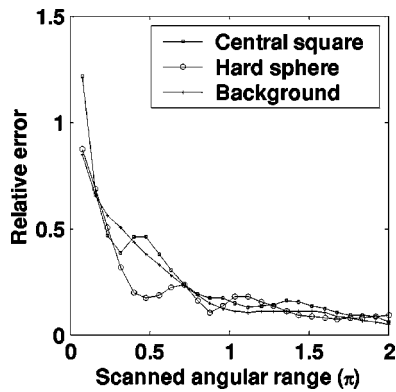


FIG. 9. The dependence of the relative errors of the mean values in the hard sphere (circle markers), the central square (square markers), and the background (asterisks) on the scanned angular range.

case of the background (because its real value is zero). When the scanned angular range is less than  $\pi$ , the errors decrease sharply with the increasing scanned angular range. On the other hand, when the scanned angular range is larger than  $\pi$ , the errors change much more slowly as the scanned angular range increases. The results agree with our theoretical conclusions. However, there are some fluctuations added to the trends of the curves. By comparing the three curves in Fig. 9, we find that these fluctuations depend strongly on the location of the object with respect to the detection curve. A more extensive study is needed to understand these fluctuations. There are some residual errors even in the full-view detection in Fig. 9. This is because we use an approximate back-projection algorithm, which is widely employed in experiments due to its better computation efficiency and stability when compared to the more accurate iteration algorithms.

#### D. Experimental results

The experimental setup is described in our previous paper and will not be repeated here.<sup>6</sup> The sample and the polar coordinate system describing the scanning orbit are shown in Fig. 10(a). The sample consists of a muscle cylinder of 4 mm in diameter and 5 mm in length embedded in a chunk of pork fat of 1.2 cm in radius  $r_f$ . There is a 10-mm fat layer below the muscle and another 7-mm one above it. An electromagnetic pulse is delivered to the sample from below (i.e., from behind the picture plane). With a scanning radius of  $r_d = 7.1$  cm, thermoacoustic data are collected around the sample over a  $2\pi$  angular span with 161 steps. As it is mentioned above, the electromagnetic pulse profile and the impulse response function of the ultrasonic transducer impose a filter on the thermoacoustic signals. We attempted to correct this effect using deconvolution but found that the resulted images were distorted, due to the lack of precise knowledge of the filter. Therefore, we do not use deconvolution in the reconstruction. This leads, as is explained above, to somewhat emphasized interfaces.

Figures 10(b)–10(d) show the reconstructed images using FBP with three sets of data. In the first of them, we choose the data collected along a circular detector arc of 92 degrees

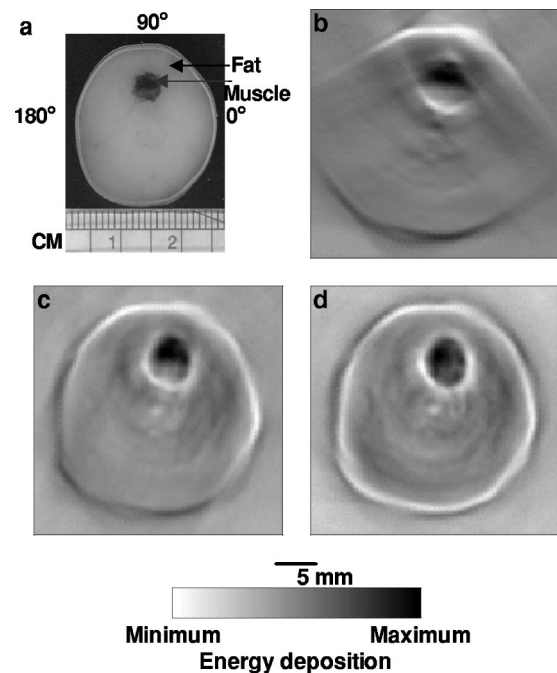


FIG. 10. (a) A photograph of the experimental sample. (b)–(d) TAT reconstructions using detection arcs of 92 degrees [from  $50^\circ$  to  $142^\circ$  in (a)], 202 degrees (from  $-18^\circ$  to  $184^\circ$ ), and 360 degrees, respectively. The blurred parts of the boundaries in (b) due to the limited view agree with the theoretical predictions. In (c) all the boundaries are resolved, since the object fits into the “detection region.”

located at the top of the picture and almost symmetric with respect to its vertical axes. One sees that the left and right boundaries of the muscle cylinder and of the pork chunk are blurred away, since their normal lines do not touch the detector arc, while the rest of the boundary is sharp. The next figure shows reconstruction obtained with the data collected from a 202-degree arc [which is about  $180 + 2 \cdot a \sin(r_f/r_d)$  obtained in the same way as  $\theta$  in Fig. 6], when the whole phantom fits into the detection region. All boundaries are sharp now. Finally, the last figure shows the reconstruction with the full-view data.

Notice that although no local reconstruction algorithms are applied, the boundaries are somewhat emphasized. The reason for this is the presence in the data of the impulse response function of the ultrasonic transducer, which has an effect similar to the application of an additional derivative with respect to the radius of the circle of integration. The presence of such a derivative emphasizes high frequencies and makes the reconstruction similar to a version of a local tomography algorithm.

#### E. Discussion

As mentioned above, although circular scanning is used in both our numerical and experimental studies, our conclusions can be applied to other configurations as well. In TAT with a planar configuration,<sup>18,31–33</sup> detections are implemented on a part of a line or a plane where the scanning view is quite limited; consequently, artifacts and interface blurring appear in the reconstructed images. In fact, in planar and

linear scanning geometries one can never have an object immersed entirely into the “detection region” because the normal lines to any interfaces that are orthogonal to the detector plane (line) never pass through a detector. As a consequence, those parts of the interfaces will be blurred in any kind of reconstruction. For a sufficiently large view, these parts will be small, but theoretically will never disappear. For example, 2-D planar detection is utilized to image artificial blood vessels;<sup>18</sup> the scanning view is about 2.18 steradians. Therefore, it is not surprising that only the interfaces more-or-less parallel to the plane of detection are well imaged. Linear scanning detection is used to image a 2-D phantom.<sup>32</sup> Because the view of the linear scanning<sup>32</sup> is much larger than that of planar scanning,<sup>18</sup> the interfaces are recovered much more completely. However, due to a limited view, artifacts and interface blurring similar to those demonstrated in our numerical and experimental studies still appear in the images.<sup>32</sup>

By comparing Figs. 7 and 10, we observe that the quality of images reconstructed from incomplete data when an object is in the detection region, is comparable with those from the full-view data. Scanning a smaller range has the advantages of reducing the scanning time or the size of the acoustic transducer array. It should be pointed out that this advantage usually exists in the case when both the sample and medium are relatively acoustically homogeneous. When strong wavefront distortion caused by acoustic heterogeneities occurs, it might be beneficial to collect the signal from all directions.

#### IV. CONCLUSIONS

It is explained theoretically what parts of the image can be stably recovered in the limited-view TAT. Analytic and algebraic reconstruction methods are developed and applied to numerical phantoms and experimental data. Both numerical and experimental results agree perfectly with the theoretical conclusions. The results can be applied practically to quantitative reconstructions with incomplete data, as well as to designing efficient scanning geometries in TAT and interpreting the obtained images.

#### ACKNOWLEDGMENTS

The work of the first two authors was sponsored in part by the U.S. Army Medical Research and Materiel Command Grant No. DAMD17-00-1-0455, the National Institutes of Health Grant No. R01 EB000712, and the Texas Higher Education Coordinating Board Grant No. ARP 000512-0063-2001. The work of the last two authors was sponsored in part by the NSF Grants No. DMS-9971674 and No. DMS-0296150.

#### APPENDIX: DERIVATION OF EQ. (5):

Equation (2) can be rewritten as

$$p_1(\mathbf{r}, t) = \frac{\beta I_0}{4\pi C} \mathbf{D}_t \frac{\mathbf{R}\varphi}{t}. \quad (\text{A1})$$

We define  $p_2(\mathbf{r}, t) = v_s \int_0^t p_1(\mathbf{r}, t) dt$ . Then we have

$$\frac{4\pi C t p_2(\mathbf{r}, t)}{\beta I_0 v_s} = \mathbf{R}\varphi. \quad (\text{A2})$$

If the detector is not very close to the objects, we can approximate the circular radon transform by the standard radon transform. The forward and inverse formulas for the standard radon transform are<sup>15</sup>

$$m(s, \theta) = \int_{\mathbf{r} \cdot \boldsymbol{\theta} = s} f(\mathbf{r}) d\mathbf{r}, \quad (\text{A3})$$

and

$$f(\mathbf{r}) = \frac{1}{4\pi} \int_0^{2\pi} d\theta \mathbf{H} \frac{\partial m(\mathbf{r} \cdot \boldsymbol{\theta}, \theta)}{\partial s}, \quad (\text{A4})$$

where  $\mathbf{H}$  is the Hilbert transform. Although the circular radon transform is different, one can write down an approximate inversion formula modeled after Eq. (A4). By combining an analog of Eq. (A4) with Eq. (A2), one obtains an approximate formula,

$$\varphi(\mathbf{r}) \approx \frac{C}{\beta I_0 v_s^2} \int_0^{2\pi} d\theta \mathbf{H} (p_1(\mathbf{r}_\theta, |\mathbf{r}_\theta - \mathbf{r}|/v_s) |\mathbf{r}_\theta - \mathbf{r}| + p_2(\mathbf{r}_\theta, |\mathbf{r}_\theta - \mathbf{r}|)), \quad (\text{A5})$$

where  $\theta$  is defined as in Fig. 4. According to Fig. 4, we have the relation

$$d\theta = ds \frac{\mathbf{n} \cdot (\mathbf{r} - \mathbf{r}_\theta)}{|\mathbf{r} - \mathbf{r}_\theta|^2}, \quad (\text{A6})$$

where  $\mathbf{n}$  is the inward normal to the detection curve at  $\mathbf{r}_\theta$  and  $ds$  is the arc length differential of the detection curve. After substituting this identity into Eq. (A5) we obtain Eq. (5). Equation (7) can be derived in a similar way.

<sup>a)</sup> Author to whom correspondence should be addressed. Telephone: 979-847-9040; fax: 979-845-4450; electronic mail: LWang@tamu.edu; URL: <http://oilab.tamu.edu>

<sup>1</sup> W. Joines, R. Jirtle, M. Rafal, and D. Schaeffer, “Microwave power absorption differences between normal and malignant tissue,” *Int. J. Radiat. Oncol. Biol. Phys.* **6**, 681–687 (1980).

<sup>2</sup> S. Chaudhary, R. Mishra, A. Swarup, and J. Thomas, “Dielectric properties of normal human breast tissues at radiowave and microwave frequencies,” *Indian J. Biochem. Biophys.* **21**, 76–79 (1984).

<sup>3</sup> W. Joines, Y. Zhang, C. Li, and R. Jirtle, “The measured electrical properties of normal and malignant human tissues from 50–900 MHz,” *Med. Phys.* **21**, 547–550 (1994).

<sup>4</sup> W. F. Cheong, S. A. Prahl, and A. J. Welch, “A review of the optical properties of biological tissues,” *IEEE J. Quantum Electron.* **26**, 2166–2185 (1990).

<sup>5</sup> Y. Xu, D. Feng, and L.-H. V. Wang, “Exact frequency-domain reconstruction for thermoacoustic tomography: I. Planar geometry,” *IEEE Trans. Med. Imaging* **21**, 823–828 (2002).

<sup>6</sup> M. Xu and L.-H. V. Wang, “Time-domain reconstruction for thermoacoustic tomography in a spherical geometry,” *IEEE Trans. Med. Imaging* **21**, 814–822 (2002).

<sup>7</sup> Y. Xu, M. Xu, and L.-H. V. Wang, “Exact frequency-domain reconstruction for thermoacoustic tomography: II. Cylindrical geometry,” *IEEE Trans. Med. Imaging* **21**, 829–833 (2002).

<sup>8</sup> R. A. Kruger, P. Liu, Y. R. Fang, and C. R. Appledorn, “Photoacoustic ultrasound (PAUS)—reconstruction tomography,” *Med. Phys.* **22**, 1605–1609 (1995).

- <sup>9</sup>C. G. A. Hoelen, F. F. M. Mul, R. Pongers, and A. Dekker, "Three-dimensional photoacoustic imaging of blood vessels in tissue," *Opt. Lett.* **23**, 648–650 (1998).
- <sup>10</sup>J. A. Fawcett, "Inversion of  $n$ -dimensional spherical averages," *SIAM (Soc. Ind. Appl. Math.) J. Appl. Math.* **45**, 336–341 (1985).
- <sup>11</sup>L.-E. Andersson, "On the determination of a function from spherical averages," *SIAM (Soc. Ind. Appl. Math.) J. Math. Anal.* **19**, 214–232 (1988).
- <sup>12</sup>S. Nilsson, "Application of fast backprojection techniques for some inverse problems of integral geometry," Linköping Studies in Science and Technology, Dissertation 499, Department of Mathematics, Linköping University, Linköping, Sweden, 1997.
- <sup>13</sup>A. Denisjuk, "Integral geometry on the family of semi-spheres," *Fract. Calc. Appl. Anal.* **2**, 31–46 (1999).
- <sup>14</sup>V. P. Palamodov, "Reconstruction from limited data of arc means," *J. Fourier Anal. Appl.* **6**, 25–42 (2000).
- <sup>15</sup>F. Natterer and F. Wuebbeling, *Mathematical Methods in Image Reconstruction* (SIAM, Philadelphia, PA, 2001), Sect. 2.5.3.
- <sup>16</sup>K. P. Köstli, M. Frenz, H. Bebie, and H. P. Weber, "Temporal backward projection of optoacoustic pressure transients using Fourier transform methods," *Phys. Med. Biol.* **46**, 1863–1872 (2001).
- <sup>17</sup>S. J. Norton and M. Linzer, "Ultrasonic reflectivity imaging in three dimensions: exact inverse scattering solution for plane, cylindrical and spherical aperture," *IEEE Trans. Biomed. Eng.* **BME-28**, 202–220 (1981).
- <sup>18</sup>C. G. A. Hoelen and F. F. M. Mul, "Image reconstruction for photoacoustic scanning of tissue structures," *Appl. Opt.* **39**, 5872–5883 (2001).
- <sup>19</sup>A. H. Delaney and Y. Bresler, "Globally convergent edge-preserving regularized reconstruction: an application to limited-angle tomography," *IEEE Trans. Image Process.* **7**, 204–221 (1998).
- <sup>20</sup>X. Pan and M. Anastasio, "Minimum-scan filtered backpropagation algorithms in diffraction tomography," *J. Opt. Soc. Am.* **16**, 2896–2903 (1999).
- <sup>21</sup>X. Pan, Y. Zou, and M. Anastasio, "Data redundancy and reduced-scan reconstruction in reflectivity tomography," *IEEE Trans. Image Process.* **12**, 784–795 (2003).
- <sup>22</sup>M. L. Agranovsky and E. T. Quinto, "Injectivity sets for the radon transform over circles and complete systems of radial functions," *J. Funct. Anal.* **139**, 383–413 (1996).
- <sup>23</sup>A. K. Louis and E. T. Quinto, "Local tomographic methods in sonar," in *Surveys on Solution Methods for Inverse Problems* (Springer-Verlag, Vienna, 2000), pp. 147–154.
- <sup>24</sup>E. T. Quinto, "Singularities of the x-ray transform and limited data tomography in  $\mathbb{R}^2$  and  $\mathbb{R}^3$ ," *SIAM J. Math. Anal.* **24**, 1215–1225 (1993).
- <sup>25</sup>A. Faridani, E. L. Ritman, and K. T. Smith, "Local tomography," *SIAM (Soc. Ind. Appl. Math.) J. Appl. Math.* **52**, 459–484 (1992).
- <sup>26</sup>A. Faridani, E. L. Ritman, and K. T. Smith, "Local tomography. Examples of local tomography," *SIAM (Soc. Ind. Appl. Math.) J. Appl. Math.* **52**, 1193–1198 (1992).
- <sup>27</sup>A. Faridani, D. V. Finch, E. L. Ritman, and K. Smith, "Local tomography II," *SIAM (Soc. Ind. Appl. Math.) J. Appl. Math.* **57**, 1095–1127 (1997).
- <sup>28</sup>P. Kuchment, K. Lancaster, L. Mogilevskaya, and M. Mogilevsky, "On local tomography," *Inverse Probl.* **11**, 571–589 (1995).
- <sup>29</sup>V. Isakov, *Inverse Problems for Partial Differential Equations*, Applied Mathematical Science (Springer-Verlag, Berlin, 1998), Vol. 127.
- <sup>30</sup>G. Beylkin, "The inversion problem and applications of the generalized radon transform," *Commun. Pure Appl. Math.* **37**, 579–599 (1984).
- <sup>31</sup>G. Ku and L.-H. V. Wang, "Scanning microwave-induced thermoacoustic tomography: signal, resolution, and contrast," *Med. Phys.* **28**, 4–10 (2001).
- <sup>32</sup>D. Feng, Y. Xu, G. Ku, and L.-H. V. Wang, "Microwave-induced thermoacoustic tomography: reconstruction by synthetic aperture," *Med. Phys.* **28**, 2427–2431 (2001).
- <sup>33</sup>C. G. A. Hoelen, R. Pongers, G. Hamhuis, F. F. M. Mul, and J. Greve, "Photoacoustic blood cell detection and imaging of blood vessels in phantom tissue," *SPIE* **3196**, 142–153 (1998).